Research Square

Preprints are preliminary reports that have not undergone peer review.
They should not be considered conclusive, used to inform clinical practice,
or referenced by the media as validated information.

Synthesis and Characterization of PVA/rGO Composite Hydrogel for Efficient Removal of Dyes and Heavy Metals from Aqueous Solutions

Sahil Yousuf

sahilyousuf_2024mscphy007@nitsri.ac.in

National Institute of Technology, Srinagar https://orcid.org/0009-0009-6462-7404

Research Article

Keywords: PVA hydrogel, reduced graphene oxide, adsorption, methylene blue, Congo Red, heavy metals, freeze–thaw, water purification

Posted Date: July 14th, 2026

DOI: https://doi.org/10.21203/rs.3.rs-10337220/v1

License: This work is licensed under a Creative Commons Attribution 4.0 International License.
Read Full License

Additional Declarations: The authors declare no competing interests.

Synthesis and Characterization of PVA/rGO Composite Hydrogel for Efficient Removal of Dyes and Heavy Metals from Aqueous Solutions

Sahil Yousuf

Department of Physics, National Institute of Technology Srinagar, Jammu & Kashmir 190006, India

Abstract

The widespread discharge of synthetic dyes and toxic heavy metal ions into aquatic environments has become a critical environmental challenge due to its adverse effects on ecosystems and human health. In this work, a polyvinyl alcohol/reduced graphene oxide (PVA/rGO) composite hydrogel was successfully fabricated through a simple aqueous blending strategy using borax as a crosslinking agent followed by repeated freeze–thaw treatment. The physicochemical characteristics of the prepared hydrogel were systematically investigated by X-ray diffraction (XRD), Fourier-transform infrared (FTIR) spectroscopy, Raman spectroscopy, scanning electron microscopy (SEM), Brunauer–Emmett–Teller (BET) surface area analysis, and thermogravimetric analysis (TGA). Characterization confirmed the uniform incorporation of rGO nanosheets within the PVA matrix, producing a porous three-dimensional architecture with improved thermal stability and increased surface area.

The adsorption performance of the composite hydrogel was evaluated toward methylene blue (MB), Congo Red (CR), and selected heavy metal ions (Pb^{2+}, Cu^{2+}, and Cd^{2+}) under batch conditions. The maximum adsorption capacities reached 185.6 $mg\,g^{-1}$ for MB, 142.3 $mg\,g^{-1}$ for CR, 98.7 $mg\,g^{-1}$ for Pb^{2+}, 76.4 $mg\,g^{-1}$ for Cu^{2+}, and 62.1 $mg\,g^{-1}$ for Cd^{2+}, demonstrating the excellent affinity of the hydrogel for both organic dyes and metal contaminants. Equilibrium studies showed that the Langmuir isotherm ad-

*Corresponding author

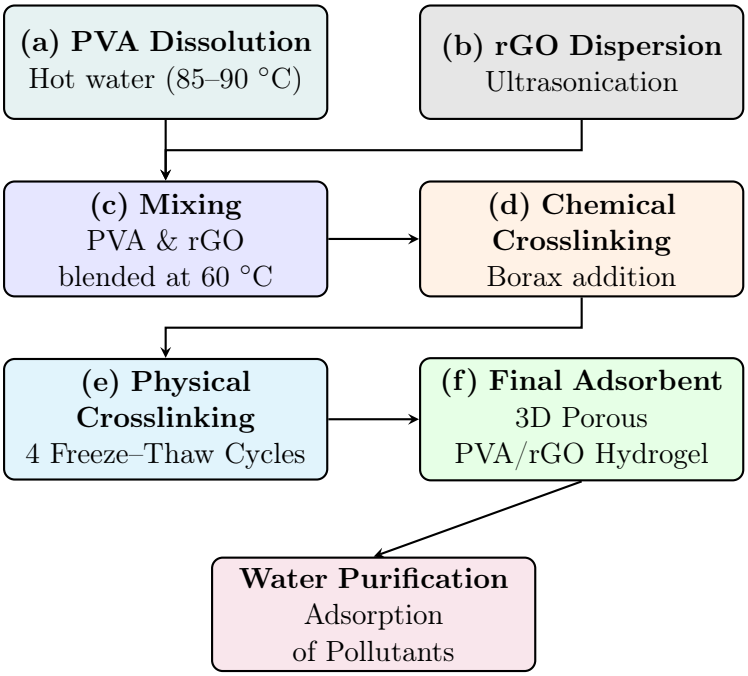
Email address: sahilyousuf_2024mscphy007@nitsri.ac.in (Sahil Yousuf)

equately described the adsorption of MB and the investigated heavy metal ions, whereas CR adsorption exhibited better agreement with the Freundlich model. Adsorption kinetics for all pollutants followed the pseudo-second-order model, suggesting that chemisorption predominated during the uptake process. The overall adsorption behavior is attributed to the combined effects of π–π stacking interactions, hydrogen bonding, electrostatic attraction, and surface complexation between the pollutants and the functional groups present on the composite hydrogel.

Furthermore, the PVA/rGO hydrogel retained more than 85% of its original adsorption efficiency after six successive adsorption–desorption cycles, highlighting its excellent structural stability and regeneration capability. Owing to its straightforward fabrication, high adsorption capacity, and outstanding reusability, the developed PVA/rGO composite hydrogel represents a promising and economically viable adsorbent for the efficient treatment of dye- and heavy metal-contaminated wastewater.

Keywords: PVA hydrogel; reduced graphene oxide; adsorption; methylene blue; Congo Red; heavy metals; freeze–thaw; water purification

---



Graphical Abstract: Schematic illustration of PVA/rGO composite hydrogel synthesis: (a) dissolution of PVA in water; (b) dispersion of rGO nanosheets; (c) mixing of PVA and rGO; (d) crosslinking with borax through borate ester linkages; (e) freeze–thaw cycling inducing physical crosslinking; and (f) the final 3D porous network applied for the removal of dyes and heavy metals.

1. Introduction

The increasing demand for industrial production and accelerated urban development have substantially intensified the discharge of hazardous pollutants into aquatic ecosystems, making water contamination a critical environmental issue worldwide [1]. Among the available wastewater treatment technologies, adsorption has attracted considerable interest because of its operational simplicity, high removal efficiency, economic feasibility, and ease of adsorbent regeneration [2, 3]. Nevertheless, the growing release of synthetic dyes and toxic heavy metal ions from industrial activities continues to threaten both environmental sustainability and public health due to their persistence, toxicity, and tendency to bioaccumulate within biological systems [4, 5]. Major industrial sectors, including textile manufacturing, leather processing, paper production, mining, electroplating, and battery fabrication, are recognized as significant sources of dye-laden effluents and heavy metal contamination [6].

Among organic contaminants, methylene blue (MB) is a widely used cationic dye employed in textile processing and biological staining. Although useful in industrial and laboratory applications, excessive discharge of MB into water bodies may result in adverse health effects, including respiratory complications, ocular irritation, and neurological disturbances [7]. Congo Red (CR), a representative anionic azo dye, exhibits exceptional chemical stability and resistance to biodegradation, while prolonged exposure has been associated with carcinogenic and mutagenic effects [8]. In addition, toxic heavy metal ions such as Pb^{2+}, Cu^{2+}, and Cd^{2+} are of particular concern because they are non-biodegradable and readily accumulate in living organisms, causing severe disorders affecting the nervous system, kidneys, liver, and other vital organs [9].

A variety of physicochemical treatment methods have been proposed to eliminate these contaminants from wastewater, including chemical precipitation, membrane separation, electrochemical treatment, ion exchange, advanced oxidation, and adsorption [2]. Among these approaches, adsorption remains one of the most practical and efficient technologies owing to its high treatment efficiency, straightforward operation, relatively low cost, and suitability for regeneration and repeated use [3]. The effectiveness of adsorption, however, depends strongly on the physicochemical characteristics of the adsorbent, particularly its surface area, pore architecture, abundance of active functional groups, and affinity toward target pollutants.

Hydrogels have emerged as an attractive class of adsorbent materials because of their highly porous three-dimensional polymeric networks and exceptional water-retention capability [10]. Polyvinyl alcohol (PVA) is one of the most extensively investigated hydrogel-forming polymers due to its excellent biocompatibility, non-toxicity, hydrophilicity, chemical resistance, and favorable mechanical properties [11]. Depending on the preparation method, PVA molecules can form stable hydrogel networks through either physical interactions or chemical crosslinking, generating interconnected porous structures suitable for adsorption applications [12]. Nevertheless, pristine PVA hydrogels generally possess relatively limited adsorption capacity because of the insufficient number of chemically active adsorption sites.

To overcome these limitations, numerous studies have focused on incorporating nanostructured materials into polymer matrices to improve adsorption efficiency [13]. Among the available nanomaterials, graphene oxide (GO) and reduced graphene oxide (rGO) have attracted exceptional attention because of their two-dimensional morphology, large specific surface area, outstanding mechanical strength, and rich surface chemistry [14]. Their surfaces contain oxygen-containing functional groups capable of interacting with pollutants through hydrogen bonding, π–π interactions, electrostatic attraction, and surface complexation, thereby significantly enhancing adsorption performance [15]. Consequently, GO- and rGO-based hydrogel composites have demonstrated excellent removal efficiencies for a broad range of organic dyes and heavy metal ions in aqueous media [16, 17, 18].

Integrating rGO nanosheets within a PVA hydrogel matrix combines the desirable properties of both constituents and generates a multifunctional adsorbent with improved physicochemical characteristics. The hydrophilic PVA framework facilitates rapid water penetration and pollutant diffusion, whereas rGO contributes abundant adsorption sites and increased surface area. Furthermore, borax-induced crosslinking together with repeated freeze–thaw treatment strengthens the hydrogel network, improving its structural integrity, thermal stability, and resistance to repeated adsorption–desorption operations [19]. Although several graphene-based hydrogel systems have been reported, comprehensive investigations addressing the simultaneous removal of cationic dyes, anionic dyes, and multiple heavy metal ions using PVA/rGO composite hydrogels remain comparatively scarce.

In the present study, a PVA/rGO composite hydrogel was synthesized through a straightforward aqueous-route process employing borax as the crosslinking agent and repeated freeze–thaw cycles to obtain a mechanically

robust porous structure. The prepared composite was comprehensively characterized using X-ray diffraction (XRD), Fourier-transform infrared spectroscopy (FTIR), Raman spectroscopy, scanning electron microscopy (SEM), Brunauer–Emmett–Teller (BET) surface area analysis, and complementary physicochemical techniques. Its adsorption performance toward methylene blue, Congo Red, and representative heavy metal ions (Pb^{2+}, Cu^{2+}, and Cd^{2+}) was systematically investigated under different operating conditions. Equilibrium and kinetic models were employed to elucidate the adsorption mechanism, while repeated adsorption–desorption experiments were performed to evaluate the regeneration capability and long-term applicability of the developed composite hydrogel for wastewater purification.

2. Materials and Methods

2.1. Materials

Polyvinyl alcohol (PVA; molecular weight 89,000–98,000 g mol^{-1}; degree of hydrolysis 98–99%) was procured from Sigma-Aldrich. Reduced graphene oxide (rGO) nanosheets, consisting of approximately 2–5 graphene layers with lateral dimensions of 1–5 μm and a specific surface area exceeding 500 m^2 g^{-1}, were supplied by Graphene Laboratories Inc. Sodium tetraborate decahydrate (borax, $Na_2B_4O_7 \cdot 10H_2O$, ACS grade) together with $Pb(NO_3)_2$, $CuSO_4 \cdot 5H_2O$, and $CdCl_2 \cdot 2.5H_2O$ were purchased from Merck. Methylene blue (MB; $C_{16}H_{18}ClN_3S{\cdot}3H_2O$, molecular weight 373.9 g mol^{-1}) and Congo Red (CR; $C_{32}H_{22}N_6Na_2O_6S_2$, molecular weight 696.7 g mol^{-1}) were obtained from HiMedia Laboratories. All reagents were of analytical grade and employed directly without additional purification. Double-distilled water served as the solvent for all synthesis and adsorption experiments.

2.2. Synthesis of PVA/rGO Composite Hydrogel

The PVA/rGO composite hydrogel was fabricated through a combined chemical and physical crosslinking strategy. Prior optimization experiments established that the optimum formulation consisted of 2.0 g PVA, 0.10 g rGO, 0.15 g borax, and 20 mL distilled water.

1. **Preparation of the PVA solution:**
   Initially, 2.0 g of PVA powder was gradually introduced into 20 mL of distilled water under continuous stirring at ambient temperature. The suspension was subsequently heated to 85–90°C while stirring at

500 rpm for 45 min until complete dissolution produced a homogeneous, transparent, and highly viscous polymer solution. Before incorporation of rGO, the solution temperature was reduced to approximately 60–70°C.

2. **Preparation of the rGO dispersion:**
   A quantity of 100 mg rGO powder was dispersed in 15 mL distilled water and treated in an Elmasonic P60H ultrasonic bath (37 kHz, 150 W) for 60 min at room temperature. Ultrasonication effectively separated the graphene sheets and generated a stable, uniformly dispersed black suspension without visible particle agglomeration.
3. **Formation of the polymer–nanofiller mixture:**
   The pre-cooled PVA solution was introduced slowly into the ultrasonicated rGO suspension while stirring continuously at 600 rpm and maintaining the temperature at 60°C. Mixing was continued for an additional 45 min to promote homogeneous distribution of the graphene nanosheets throughout the polymer matrix and to facilitate intermolecular interactions between PVA chains and rGO surfaces.
4. **Chemical crosslinking:**
   Borax (0.15 g) was first dissolved in 3 mL of warm distilled water maintained at approximately 60°C. The resulting solution was then added dropwise into the PVA/rGO mixture under vigorous stirring at 800 rpm. Immediately after addition, the viscosity increased noticeably, indicating the initiation of gel formation through borate-mediated crosslinking. Stirring was maintained for another 15 min to ensure uniform development of the crosslinked network.
5. **Freeze–thaw treatment:**
   The freshly prepared gel precursor was transferred into cylindrical polyethylene moulds (diameter 2.5 cm; height 3.0 cm) and subjected to repeated freeze–thaw processing. Each cycle consisted of freezing at −20°C for 12 h followed by thawing at 25°C for 4 h. Four consecutive cycles were employed to strengthen the physically crosslinked network through the formation of stable crystalline domains within the PVA matrix. Repeated freeze–thaw treatment also contributed to the development of an interconnected porous architecture that is advantageous for subsequent adsorption applications.
6. **Purification and storage:**
   After completion of the freeze–thaw cycles, the hydrogels were carefully removed from the moulds and repeatedly washed with fresh distilled

water to eliminate any remaining soluble reagents or loosely attached species. Washing was performed six times over a period of 24 h. The purified hydrogels were finally immersed in distilled water and stored at 4°C until characterization and adsorption experiments were carried out.

For comparison, pristine PVA hydrogels were prepared following the identical synthesis procedure without the addition of rGO. Furthermore, composite hydrogels containing different rGO loadings (0.5, 1.0, 2.0, 3.0, and 5.0 wt% with respect to PVA) were fabricated under identical processing conditions to determine the optimum graphene content for adsorption performance.

2.3. Characterization Techniques

A combination of structural, spectroscopic, microscopic, surface, thermal, and analytical techniques was employed to comprehensively evaluate the physicochemical characteristics of the synthesized PVA/rGO composite hydrogel.

2.3.1. X-ray Diffraction (XRD)

The crystalline structure of the prepared materials was investigated using a Rigaku SmartLab X-ray diffractometer operating with Cu Kα radiation (λ = 1.5406 Å) at an accelerating voltage of 40 kV and a tube current of 40 mA. Before analysis, freeze-dried hydrogel specimens were finely pulverized to obtain homogeneous powders. Diffraction patterns were collected over a 2θ interval of 5–60° using a scanning step of 0.02° and a scanning rate of 2° min^{-1}. The resulting diffraction peaks were indexed by comparison with standard reference data, while the degree of crystallinity was estimated from integrated peak areas using the conventional peak-area approach.

2.3.2. Fourier-Transform Infrared Spectroscopy (FTIR)

The surface functional groups and chemical bonding characteristics of the samples were examined using a PerkinElmer Spectrum Two FTIR spectrometer equipped with a universal attenuated total reflectance (ATR) accessory. Spectra were acquired within the wavenumber region of 4000–400 cm^{-1} at a spectral resolution of 4 cm^{-1}. Each spectrum represented the average of 64 consecutive scans to improve the signal-to-noise ratio. Prior to interpretation, all spectra were baseline corrected and normalized using the Spectrum software package.

2.3.3. Raman Spectroscopy

Raman measurements were carried out using a Horiba LabRAM HR Evolution Raman spectrometer fitted with a 532 nm excitation laser operating at 20 mW. Spectral acquisition employed an 1800 grooves mm^{-1} diffraction grating over the range of 800–3200 cm^{-1}, providing an approximate spectral resolution of 1 cm^{-1}. Five individual spectra, each recorded with an exposure time of 30 s, were accumulated for every sample to improve spectral quality. Baseline correction and Lorentzian peak deconvolution were subsequently performed to obtain accurate peak positions and intensity ratios.

2.3.4. Scanning Electron Microscopy (SEM)

The morphology and internal pore architecture of the freeze-dried hydrogels were examined using a Zeiss EVO 18 scanning electron microscope operated at an accelerating voltage of 10 kV. To minimize electrostatic charging during imaging, each specimen was coated with an approximately 5 nm thick conductive gold layer using a Quorum Q150T ES sputter coater. Micrographs were collected over a magnification range of 100× to 10,000×, allowing detailed observation of both the overall porous framework and the fine structural features of the pore walls.

2.3.5. Brunauer–Emmett–Teller (BET) Surface Area Analysis

Specific surface area and pore characteristics were determined from nitrogen adsorption–desorption measurements performed at 77 K using a Micromeritics ASAP 2020 surface area analyzer. Approximately 0.1 g of freeze-dried hydrogel was vacuum degassed at 105°C for 12 h prior to analysis to eliminate physically adsorbed moisture and volatile species. Surface area values were calculated according to the Brunauer–Emmett–Teller (BET) model, whereas pore-size distributions were derived from the desorption isotherms using the Barrett–Joyner–Halenda (BJH) method.

2.3.6. Thermogravimetric Analysis (TGA)

Thermal degradation behaviour was investigated using a PerkinElmer TGA 4000 thermogravimetric analyzer. Approximately 5 mg of freeze-dried material was heated from 30 to 800°C at a constant heating rate of 10°C min^{-1} under a continuous nitrogen atmosphere maintained at a flow rate of 20 mL min^{-1}. The recorded thermograms were used to evaluate characteristic decomposition stages, thermal stability, and the residual char remaining after high-temperature treatment.

2.3.7. UV–Visible Spectroscopy

Residual dye concentrations during adsorption experiments were quantified using a Shimadzu UV–2600 UV–Visible spectrophotometer equipped with 1 cm quartz cuvettes. Methylene blue concentration was determined from its characteristic absorption maximum at 664 nm, whereas Congo Red was monitored at 497 nm. Quantitative analysis was performed using calibration curves established over the concentration interval of 0.5–50 mg L^{-1} for each dye.

2.3.8. Atomic Absorption Spectroscopy (AAS)

The concentrations of dissolved Pb^{2+}, Cu^{2+}, and Cd^{2+} ions were measured using a PerkinElmer AAnalyst 400 atomic absorption spectrometer fitted with element-specific hollow cathode lamps. Instrument calibration was carried out using certified standard reference solutions prior to sample analysis. The analytical detection limits were determined to be 0.01 mg L^{-1} for Pb^{2+}, 0.005 mg L^{-1} for Cu^{2+}, and 0.002 mg L^{-1} for Cd^{2+}, ensuring reliable quantification throughout the adsorption experiments.

2.4. Adsorption Experiments

Batch adsorption experiments were performed to evaluate the removal efficiency of the synthesized PVA/rGO composite hydrogel toward organic dyes and heavy metal ions. Unless otherwise specified, all measurements were carried out at 25 ± 1°C. Each experiment was independently repeated three times, and the reported values represent the arithmetic mean together with the corresponding standard deviation.

2.4.1. Effect of pH

The influence of solution pH on adsorption performance was systematically examined by adjusting the initial pH of the pollutant solutions between 2.0 and 10.0 using 0.1 M HCl or 0.1 M NaOH. Initial concentrations were fixed at 50 mg L^{-1} for methylene blue (MB) and Congo Red (CR), whereas each heavy metal ion solution (Pb^{2+}, Cu^{2+}, and Cd^{2+}) was prepared at 20 mg L^{-1}. For every experiment, 20 mg of hydrogel was introduced into 50 mL of dye solution, while 50 mg of hydrogel was employed for heavy metal adsorption. The suspensions were agitated continuously at 150 rpm for 24 h to ensure equilibrium was attained. After equilibration, the final solution pH was measured and recorded before concentration analysis.

The equilibrium adsorption capacity was calculated according to:

$$q_e = \frac{(C_0 - C_e)V}{m} \tag{1}$$

where q_e (mg g^{-1}) represents the adsorption capacity at equilibrium, C_0 and C_e (mg L^{-1}) denote the initial and equilibrium pollutant concentrations, respectively, V (L) is the solution volume, and m (g) is the mass of the adsorbent employed in each experiment.

The pH investigation provides valuable information regarding the influence of surface charge and pollutant speciation on adsorption behaviour, thereby assisting in identifying the optimum operating conditions for subsequent equilibrium and kinetic studies.

2.4.2. Adsorption Isotherms

Adsorption equilibrium studies were carried out by varying the initial pollutant concentration while maintaining a constant amount of adsorbent. For MB and CR, initial concentrations ranged from 10 to 300 mg L^{-1} using 20 mg of hydrogel dispersed in 50 mL of solution. In the case of Pb^{2+}, Cu^{2+}, and Cd^{2+}, concentration levels between 5 and 200 mg L^{-1} were investigated with 50 mg of hydrogel in the same solution volume. All suspensions were shaken at 150 rpm for 24 h to establish adsorption equilibrium. Following separation of the adsorbent, the equilibrium concentrations were determined experimentally, and adsorption capacities were calculated using Eq. (1).

To describe the adsorption behaviour, the equilibrium data were analyzed using both the Langmuir and Freundlich adsorption models, allowing assessment of surface homogeneity and adsorption characteristics.

The Langmuir model assumes adsorption occurs through the formation of a single molecular layer on energetically equivalent adsorption sites and is expressed as

$$q_e = \frac{q_{\max} K_L C_e}{1 + K_L C_e} \tag{2}$$

where $q_{\max}$ (mg g^{-1}) denotes the maximum monolayer adsorption capacity, while K_L (L mg^{-1}) is the Langmuir equilibrium constant related to the affinity between the adsorbate and the adsorbent.

The Freundlich equation, which is widely applied to heterogeneous adsorbent surfaces and multilayer adsorption processes, is given by

$$q_e = K_F C_e^{1/n} \tag{3}$$

where K_F (mg g^{-1} (L mg^{-1})$^{1/n}$) represents the Freundlich adsorption constant associated with adsorption capacity, and $1/n$ is the empirical heterogeneity parameter that reflects the adsorption intensity and surface heterogeneity of the adsorbent. Simultaneous evaluation of both models provides insight into the dominant adsorption mechanism and the nature of the interaction between pollutant species and the PVA/rGO composite hydrogel.

2.4.3. Adsorption Kinetics

The adsorption rate of the PVA/rGO composite hydrogel toward dyes and heavy metal ions was evaluated through batch kinetic experiments performed under controlled conditions. Hydrogel samples (20 mg for dye adsorption and 50 mg for heavy metal adsorption) were introduced into 50 mL of pollutant solutions containing initial concentrations of 100 mg L^{-1} for MB and CR, and 50 mg L^{-1} for Pb^{2+}, Cu^{2+}, and Cd^{2+}. The suspensions were maintained at 25°C under continuous agitation at 150 rpm.

To monitor adsorption progress, aliquots were collected after 0, 5, 10, 15, 20, 30, 45, 60, 90, 120, 180, 240, 360, 480, 720, and 1440 min. The residual pollutant concentration at each sampling interval was determined using the appropriate analytical technique, and the adsorption capacity at time t was calculated using:

$$q_t = \frac{(C_0 - C_t)V}{m} \tag{4}$$

where q_t (mg g^{-1}) is the adsorption capacity at time t, C_0 and C_t (mg L^{-1}) are the initial and instantaneous pollutant concentrations, respectively, V (L) is the solution volume, and m (g) denotes the mass of the adsorbent.

To investigate the adsorption mechanism and identify the rate-controlling step, the experimental data were analyzed using the pseudo-first-order, pseudo-second-order, and Weber–Morris intraparticle diffusion models. Comparison of these models provides valuable insight into the adsorption pathway and the relative contributions of surface reaction and mass-transfer processes.

The pseudo-first-order kinetic model proposed by Lagergren is expressed as

$$\ln(q_e - q_t) = \ln q_e - k_1 t \tag{5}$$

where k_1 (min^{-1}) is the pseudo-first-order rate constant.

The pseudo-second-order kinetic model is represented by

$$\frac{t}{q_t} = \frac{1}{k_2 q_e^2} + \frac{t}{q_e} \tag{6}$$

where k_2 (g mg^{-1} min^{-1}) denotes the pseudo-second-order rate constant.

To further evaluate the diffusion behaviour of pollutant molecules within the porous hydrogel, the Weber–Morris intraparticle diffusion model was employed:

$$q_t = k_{id} t^{1/2} + C \tag{7}$$

where k_{id} (mg g^{-1} min$^{-1/2}$) is the intraparticle diffusion rate constant, while C (mg g^{-1}) reflects the contribution of the boundary layer to the overall adsorption process. Analysis of these kinetic models enables a comprehensive assessment of adsorption rates, diffusion characteristics, and the dominant mechanism governing pollutant uptake.

2.4.4. Adsorption–Desorption and Reusability

The regeneration capability of the synthesized hydrogel was evaluated through repeated adsorption–desorption cycles. Dye-loaded samples were regenerated using 0.1 M HCl, whereas heavy metal-loaded hydrogels were treated with 0.01 M EDTA solution. Following each adsorption experiment, the hydrogel was rinsed thoroughly with distilled water to remove loosely attached species before being immersed in 50 mL of the appropriate desorbing solution.

Desorption was carried out for 2 h at room temperature under continuous shaking at 150 rpm. After regeneration, the concentration of the released pollutant was determined, and the hydrogels were repeatedly washed with distilled water until a neutral pH was obtained. The regenerated adsorbents were subsequently reused in fresh adsorption experiments for six consecutive adsorption–desorption cycles to evaluate their long-term operational stability and regeneration efficiency.

The pollutant removal efficiency was determined using the following expression:

$$\text{Removal Efficiency } (\%) = \frac{C_0 - C_e}{C_0} \times 100 \tag{8}$$

where C_0 and C_e represent the initial and equilibrium pollutant concentrations, respectively. The regeneration study provides an assessment of the

structural stability, adsorption durability, and practical reusability of the PVA/rGO composite hydrogel for repeated wastewater treatment applications.

2.5. Data Analysis

The adsorption isotherm and kinetic models were analyzed by nonlinear regression using OriginPro 2021 software employing the Levenberg–Marquardt optimization algorithm. Model suitability was evaluated from both the coefficient of determination (R^2) and the reduced chi-square (χ^2) statistics to ensure reliable parameter estimation. Experimental data are reported as mean ± standard deviation from three independent measurements. Statistical comparisons among experimental groups were performed using one-way analysis of variance (ANOVA) followed by Tukey's multiple-comparison test, and differences were considered statistically significant at $p < 0.05$.

3. Results and Discussion

3.1. Synthesis and Formation Mechanism

The fabrication of the PVA/rGO composite hydrogel relies on the complementary effects of reversible chemical crosslinking and freeze–thaw-induced physical crosslinking, producing a robust three-dimensional porous architecture suitable for adsorption applications. The complete fabrication pathway together with the proposed structural evolution of the hydrogel is illustrated in Figure 1. The synthesis can be divided into four successive stages, namely polymer dissolution, nanosheet dispersion, borax-assisted network formation, and freeze–thaw crystallization.

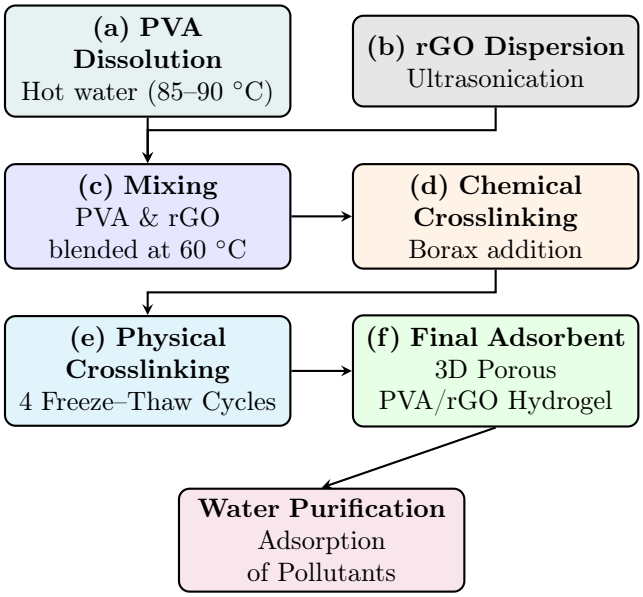


Figure 1: Schematic representation of the fabrication route for the PVA/rGO composite hydrogel. (a) Dissolution of PVA in hot water; (b) ultrasonic dispersion of rGO nanosheets; (c) homogeneous mixing of the polymer solution and rGO suspension; (d) borax-induced chemical crosslinking through borate ester formation; (e) repeated freeze–thaw cycles producing physically crosslinked crystalline domains; and (f) formation of a three-dimensional porous PVA/rGO hydrogel employed for wastewater purification.

The synthesis begins with complete dissolution of PVA in hot water, generating a uniform polymer solution in which the macromolecular chains remain highly hydrated through extensive intermolecular hydrogen bonding. Simultaneously, ultrasonic treatment effectively separates the reduced graphene oxide sheets, minimizing agglomeration and exposing residual hydroxyl, epoxy, and carboxyl functionalities across their basal planes and edges. These surface functionalities promote intimate interfacial contact with PVA chains once both suspensions are combined. Consequently, a homogeneous polymer–nanocarbon mixture is established through hydrogen bonding, van der Waals attraction, and π–π interactions between the polymer matrix and graphitic domains of rGO, ensuring efficient nanosheet dispersion throughout the precursor solution [20].

Chemical stabilization of the hydrogel network is initiated by the addition of borax. Under alkaline conditions, borate ions reversibly coordinate with vicinal hydroxyl groups on neighboring PVA chains, generating borate ester bridges that serve as permanent chemical junctions within the polymer

framework. Besides covalent borate ester formation, secondary ionic interactions between borate species and hydroxyl-rich polymer segments further strengthen the interconnected network [21]. The immediate increase in solution viscosity observed experimentally reflects rapid network development. Because these borate ester linkages are dynamic and reversible, the hydrogel possesses an adaptable internal structure capable of partial bond rearrangement, which has been associated with improved mechanical resilience, self-recovery, and pH-responsive behavior [22].

Additional structural reinforcement is achieved through successive freeze–thaw cycles. During freezing, growing ice crystals exclude polymer chains into progressively confined unfrozen regions, thereby increasing the local polymer concentration and facilitating intermolecular association. Upon thawing, these concentrated domains transform into hydrogen-bonded crystalline microregions that function as stable physical crosslinking points [23]. Repeated freeze–thaw treatment increases both the number and uniformity of these crystalline domains, resulting in improved dimensional stability and mechanical integrity while avoiding the introduction of extra chemical crosslinkers. The coexistence of reversible chemical bonds and physically crystallized regions produces a dual-crosslinked architecture that is generally more durable than networks relying on either mechanism alone.

Another important consequence of the freeze–thaw process is the development of a well-defined porous microstructure. Ice crystals formed during freezing serve as sacrificial templates, and their removal upon thawing generates interconnected macroporous channels throughout the hydrogel matrix. This hierarchical architecture provides efficient pathways for water transport and pollutant diffusion while simultaneously exposing a larger fraction of internal adsorption sites. Uniformly distributed rGO nanosheets further increase the available surface area and introduce additional adsorption-active domains through their oxygen-containing functional groups and graphitic surfaces. The cooperative interaction between the porous PVA framework and dispersed rGO therefore enhances both structural robustness and adsorption efficiency.

Overall, the fabrication strategy integrates chemical crosslinking, physical crystallization, and nanofiller reinforcement into a single interconnected network. Such structural synergy not only improves mechanical stability but also promotes rapid mass transfer, efficient utilization of adsorption sites, and long-term stability during repeated adsorption–desorption cycles. These structural advantages provide a rational basis for the superior adsorption

performance of the PVA/rGO composite hydrogel toward both organic dyes and heavy metal ions investigated in the present work.

3.2. X-ray Diffraction (XRD) Analysis

The crystal structure and phase composition of pristine PVA, reduced graphene oxide (rGO), and the fabricated PVA/rGO composite hydrogel were investigated by X-ray diffraction (XRD). The diffraction patterns obtained for the individual components and the composite are presented in Figure 2(a–c). As shown in Figure 2a, pure PVA exhibits a dominant broad diffraction peak centred at $2\theta = 19.6°$, corresponding to the (101) crystallographic plane characteristic of semi-crystalline PVA [24]. A relatively weak shoulder observed near $2\theta = 22.5°$ is assigned to the (200) reflection. The broad diffraction profile reflects the coexistence of crystalline lamellae and amorphous polymer domains within the PVA matrix. Using the standard crystallinity calculation, the crystallinity index of pristine PVA was determined to be approximately 38.5%, which agrees well with previously reported values for solution-cast PVA materials [25].

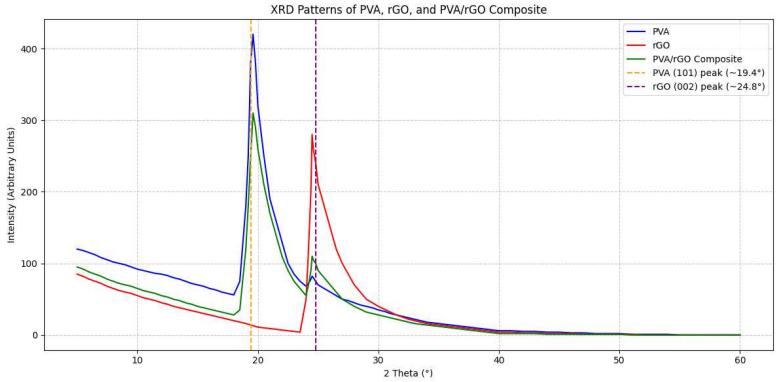


Figure 2: XRD patterns of (a) pure PVA, (b) reduced graphene oxide (rGO), and (c) the PVA/rGO composite hydrogel. The dashed line marks the characteristic PVA (101) diffraction peak, whereas the arrow indicates the rGO (002) reflection.

The diffraction spectrum of rGO (Figure 2b) displays a broad peak located at approximately $2\theta = 24.8°$, which corresponds to the (002) reflection of graphitic carbon layers [26]. Relative to pristine graphite, whose (002) reflection typically appears near $2\theta = 26.4°$, the broadened peak and slight shift indicate successful reduction of graphene oxide together with disruption

of the regular graphitic stacking. Such broadening is characteristic of turbostratic carbon structures and reflects the presence of lattice defects and residual oxygen-containing functional groups introduced during the oxidation and subsequent reduction processes. Application of Bragg's equation yielded an interlayer spacing of approximately 0.36 nm, which is slightly larger than that of crystalline graphite (0.34 nm), confirming incomplete restoration of the graphitic lattice after reduction.

The diffraction pattern of the PVA/rGO composite hydrogel (Figure 2c) demonstrates the successful integration of rGO nanosheets within the PVA network, as diffraction features associated with both components remain distinguishable. The characteristic PVA (101) reflection appears at $2\theta = 19.4°$, showing a slight shift toward lower diffraction angles compared with pristine PVA. This behaviour suggests that intermolecular interactions between the hydroxyl groups of PVA and the residual oxygen functionalities on rGO influence the packing arrangement of polymer chains and slightly modify the crystalline structure. The characteristic (002) reflection of rGO is retained at approximately $2\theta = 24.5°$, confirming that the graphene framework remains structurally intact after hydrogel fabrication. Compared with the diffraction pattern of pure rGO, the reduced intensity and increased broadening of this peak indicate effective exfoliation and homogeneous distribution of the nanosheets throughout the polymer matrix while suppressing the restacking of adjacent graphene layers.

The crystallinity index of the PVA/rGO composite hydrogel was calculated to be 33.2%, which is lower than the value obtained for pristine PVA (38.5%). The observed decrease in crystallinity results from the combined influence of rGO incorporation and borax-mediated crosslinking. Although dispersed rGO nanosheets may provide heterogeneous nucleation sites during crystallization, they simultaneously restrict the mobility of neighbouring polymer chains, thereby limiting crystal growth. In addition, hydrogen-bonding interactions established between PVA hydroxyl groups and oxygen-containing functional groups on rGO reduce the conformational freedom required for the formation of highly ordered crystalline domains. The presence of borate ester crosslinks further constrains polymer chain rearrangement, leading to an increase in the amorphous fraction of the composite. From an adsorption standpoint, this structural modification is advantageous because the larger amorphous region improves the accessibility of internal active sites and facilitates the diffusion of dye molecules and heavy metal ions throughout the interconnected hydrogel network, thereby contributing to enhanced

adsorption performance.

3.3. Fourier-Transform Infrared Spectroscopy (FTIR) Analysis

Fourier-transform infrared (FTIR) spectroscopy was employed to examine the chemical structure of the synthesized materials and to elucidate the intermolecular interactions established between PVA and rGO within the composite hydrogel. The FTIR spectra of pristine PVA, rGO, and the PVA/rGO composite are presented in Figure 3. Comparison of these spectra provides clear evidence of the successful incorporation of rGO into the polymer matrix and the formation of a chemically crosslinked hydrogel network.

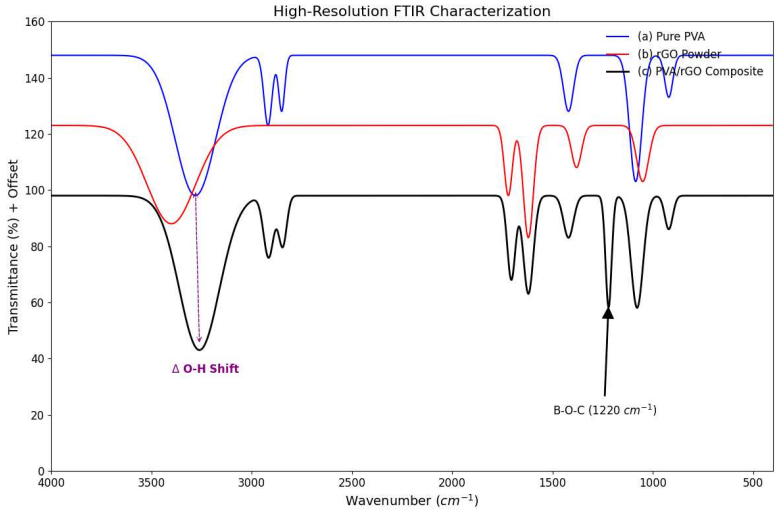


Figure 3: FTIR spectra of (a) pure PVA, (b) reduced graphene oxide (rGO), and (c) the PVA/rGO composite hydrogel. The principal absorption bands are assigned to their corresponding vibrational modes.

The spectrum of pristine PVA (Figure 3a) is characterized by a broad absorption band centred at 3280 cm^{-1}, which originates from the stretching vibration of hydroxyl (O–H) groups engaged in extensive intermolecular hydrogen bonding. The absorption bands observed at 2918 cm^{-1} and 2850 cm^{-1} are assigned to the asymmetric and symmetric stretching vibrations of aliphatic C–H bonds, respectively. A distinct band located at 1420 cm^{-1} corresponds to C–H bending vibrations of the polymer backbone. Furthermore, the intense absorption peak at 1085 cm^{-1} is attributed to C–O–C stretching

within the crystalline regions of PVA, whereas the band at 920 cm^{-1} is associated with C–O stretching vibrations originating from relatively amorphous polymer domains [27].

The FTIR spectrum of rGO (Figure 3b) confirms that a fraction of oxygen-containing functional groups remains after the reduction process. The broad absorption feature centred near 3400 cm^{-1} corresponds to O–H stretching vibrations arising from hydroxyl and carboxyl functionalities present on the graphene surface. A characteristic band at 1720 cm^{-1} is assigned to the stretching vibration of carbonyl (C=O) groups, while the absorption peak at 1620 cm^{-1} is attributed to C=C skeletal vibrations within the restored sp^2-hybridized carbon framework. Additional bands observed at 1380 cm^{-1} and 1050 cm^{-1} are associated with C–OH and epoxy (C–O–C) vibrations, respectively, demonstrating that residual oxygen functionalities remain available for subsequent interaction with the polymer matrix [28].

Significant spectral changes are observed after incorporation of rGO into the PVA matrix, confirming the formation of strong intermolecular interactions within the composite hydrogel. As shown in Figure 3c, the broad O–H stretching band shifts from 3280 cm^{-1} for pristine PVA to 3260 cm^{-1} in the composite. This shift toward lower wavenumbers indicates the strengthening of hydrogen-bonding interactions between the hydroxyl groups of PVA and the residual oxygen-containing functional groups present on the rGO nanosheets. Likewise, the C–H stretching bands appear at 2915 cm^{-1} and 2845 cm^{-1} with slight peak broadening, reflecting changes in the molecular environment of the polymer chains following rGO incorporation.

Noticeable variations are also evident in the carbonyl stretching region. Whereas pure PVA exhibits only a weak absorption band near 1710 cm^{-1} arising from residual acetate groups, the corresponding peak in the composite becomes more pronounced and shifts slightly to 1705 cm^{-1}. This behaviour suggests enhanced interactions between carbonyl-containing groups and the rGO surface, leading to a modified local chemical environment. In addition, the intensity of the C–H bending vibration at 1420 cm^{-1} decreases slightly, indicating that the incorporation of rGO influences the molecular arrangement and conformational organization of the PVA chains.

The most pronounced spectral modification occurs within the C–O–C stretching region. The characteristic PVA absorption peak shifts from 1085 cm^{-1} to 1078 cm^{-1} after composite formation and exhibits a reduction in intensity. Such changes indicate that the ether groups of PVA actively participate in intermolecular interactions with oxygen-containing functionalities

on rGO through hydrogen bonding. Furthermore, the appearance of a new absorption band at 1220 cm^{-1}, which is absent in both pristine PVA and rGO, provides direct evidence for the formation of borate ester linkages. This band is assigned to B–O–C stretching vibrations generated during borax-mediated crosslinking, thereby confirming the successful chemical stabilization of the hydrogel network [29].

Overall, the FTIR results provide compelling evidence for the successful fabrication of the PVA/rGO composite hydrogel. The observed peak shifts, intensity variations, and emergence of new absorption bands collectively demonstrate strong hydrogen-bonding interactions, effective borate ester crosslinking, and uniform incorporation of rGO within the polymer matrix. These synergistic interactions are expected to enhance the structural stability of the hydrogel while increasing the availability of active adsorption sites responsible for the efficient removal of dyes and heavy metal ions from aqueous solutions.

3.4. Raman Spectroscopy Analysis

Raman spectroscopy was employed to evaluate the structural characteristics of reduced graphene oxide (rGO) before and after its incorporation into the PVA hydrogel matrix. Owing to its high sensitivity toward graphitic ordering, lattice defects, and structural disorder, Raman analysis provides valuable insight into the integrity of carbon nanomaterials and their interaction with polymer matrices. The Raman spectra of pristine rGO and the PVA/rGO composite hydrogel recorded over the range of 800–3200 cm^{-1} are presented in Figure 4.

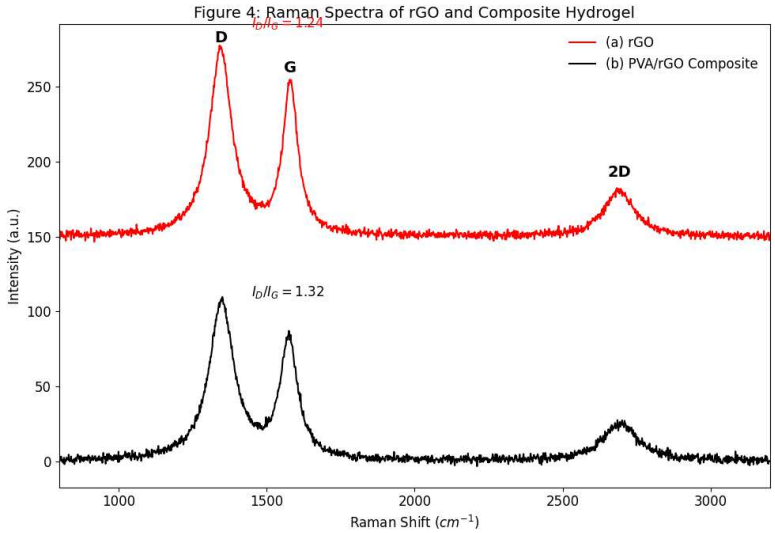


Figure 4: Raman spectra of (a) reduced graphene oxide (rGO) and (b) the PVA/rGO composite hydrogel. The characteristic D, G, and 2D bands are indicated.

The Raman spectrum of pristine rGO (Figure 4a) displays the characteristic D, G, and 2D bands commonly observed for graphene-based materials. The D band, centred at 1345 cm^{-1}, originates from the breathing vibration of aromatic sp^2 carbon rings and becomes Raman active in the presence of lattice defects, edge sites, or oxygen-containing functional groups. The G band located at 1580 cm^{-1} corresponds to the in-plane stretching vibration (E_{2g} mode) of sp^2-hybridized carbon atoms within the graphitic framework. A broad 2D band is observed at approximately 2690 cm^{-1}, arising from a second-order two-phonon scattering process that is highly sensitive to the stacking arrangement and number of graphene layers [30].

The defect density of graphitic materials is commonly evaluated using the intensity ratio of the D and G bands (I_D/I_G). For the synthesized rGO, an I_D/I_G value of 1.24 was obtained, indicating the presence of a considerable number of structural imperfections within the carbon lattice. These defects are primarily generated during the oxidation and reduction processes, where removal of oxygen functionalities is accompanied by the formation of vacancies and disruption of the extended conjugated network. Although structural defects reduce graphitic ordering, they simultaneously introduce chemically active sites that facilitate adsorption through enhanced interaction with pollutant molecules.

Following incorporation into the PVA hydrogel, the Raman spectrum of the composite (Figure 4b) retains the characteristic D, G, and 2D bands of rGO, confirming that the graphene nanosheets remain structurally preserved throughout the fabrication process. The D band is detected at 1348 cm^{-1}, whereas the G band appears at 1575 cm^{-1}, both exhibiting slight shifts relative to pristine rGO. These changes indicate modifications in the local electronic environment caused by intermolecular interactions between the dispersed graphene nanosheets and the surrounding polymer network. The calculated I_D/I_G ratio increases from 1.24 for pristine rGO to 1.32 for the composite hydrogel, suggesting a slight increase in structural disorder after composite formation. This behaviour is commonly associated with strong interfacial interactions between polymer chains and graphene sheets, as well as local strain introduced during hydrogel formation.

The 2D band is observed at approximately 2695 cm^{-1} in the composite hydrogel, exhibiting a slight shift compared with pristine rGO while maintaining its broad and asymmetric profile. Such spectral characteristics are typical of few-layer graphene and indicate that the layered structure of rGO is largely retained after incorporation into the polymer matrix. The Raman features associated with PVA are comparatively weak and are largely masked by the intense scattering response of the graphitic carbon framework, which possesses a significantly higher Raman scattering cross-section than the polymer phase.

Overall, the Raman results demonstrate the successful incorporation of rGO within the PVA hydrogel without significant degradation of its graphitic structure. The slight increase in the I_D/I_G ratio together with the minor shifts observed for the D, G, and 2D bands suggest effective interfacial interactions between rGO and PVA, accompanied by a modest increase in defect density and polymer-induced lattice strain. These structural characteristics are expected to increase the number of accessible adsorption sites while preserving the excellent physicochemical properties of the graphene nanosheets, thereby contributing to the enhanced adsorption performance of the composite hydrogel.

3.5. Scanning Electron Microscopy (SEM) Analysis

The morphology and porous architecture of the freeze-dried PVA/rGO composite hydrogel were investigated using scanning electron microscopy (SEM), and the representative micrographs are presented in Figure 5. SEM

analysis revealed a highly porous three-dimensional interconnected network characteristic of freeze–thaw fabricated hydrogels.

At low magnification (100×) (Figure 5a), the hydrogel exhibited a well-developed open-cell porous structure with uniformly distributed interconnected macropores. Quantitative image analysis of 150 individual pores showed pore diameters ranging from 128.2 to 182.5 μm, with an average pore diameter of 156.3 ± 15.8 μm. The pore size distribution was relatively narrow, with approximately 50% of the pores falling within the 130–150 μm range. The cumulative pore-size analysis confirmed a homogeneous pore structure throughout the hydrogel matrix. The overall porosity was calculated to be 72.0%, indicating the presence of substantial void volume capable of facilitating rapid mass transport during adsorption processes.

The pore morphology was predominantly circular to elliptical, exhibiting an average circularity of 0.67 and an average aspect ratio of 1.37. The interconnected pore network showed a high connectivity percentage of 94.7%, with an average connection distance of 31.5 μm. Such high connectivity is beneficial for fluid penetration and pollutant diffusion through the hydrogel matrix. The average pore wall thickness determined from 50 independent measurements was 7.92 ± 1.02 μm, with values ranging from 6.2 to 9.8 μm. The relatively uniform wall thickness indicates structural stability and mechanical integrity of the porous network.

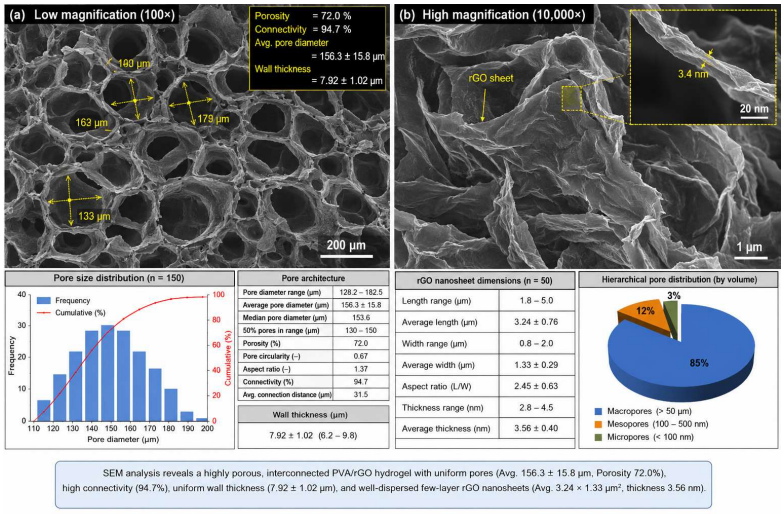
The formation of this porous architecture is attributed to the freeze–thaw processing route, where the growth of ice crystals during freezing acts as a temporary template. Upon thawing and freeze-drying, the removal of ice leaves behind a highly interconnected macroporous network. Similar ice-templated porous structures have been widely reported for hydrogel systems and are known to enhance mass transport and accessibility of adsorption sites [31].

At higher magnification (10,000×) (Figure 5b), detailed examination of the pore walls revealed the successful incorporation of reduced graphene oxide (rGO) nanosheets within the PVA matrix. The rGO sheets appeared as thin, wrinkled, and partially folded structures embedded along the pore walls and surfaces. Quantitative analysis of 50 nanosheets showed lateral dimensions ranging from 1.8 to 5.0 μm in length and 0.8 to 2.0 μm in width. The average nanosheet length and width were 3.24 and 1.33 μm, respectively, yielding an average aspect ratio of 2.45. The measured thickness of the nanosheets varied from 2.8 to 4.5 nm with an average value of 3.56 nm, confirming the presence of few-layer graphene structures.

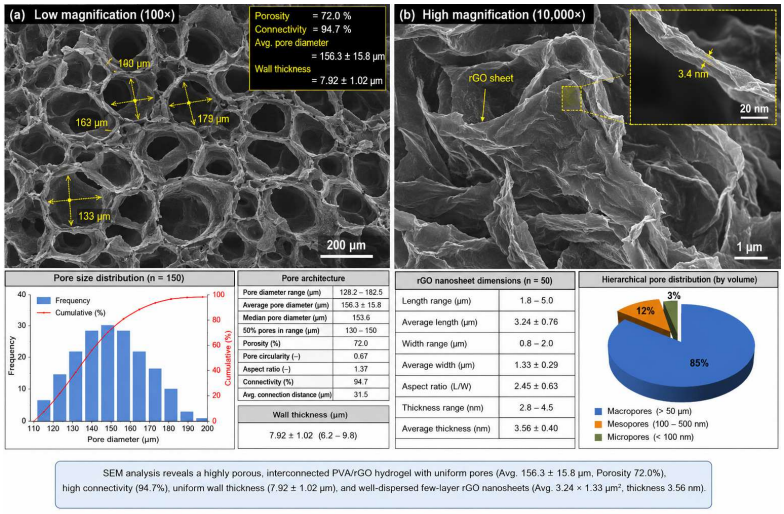
The wrinkled morphology observed for the rGO nanosheets is characteristic of reduced graphene oxide and arises from the intrinsic flexibility of two-dimensional carbon sheets and the stresses generated during freeze–thaw processing. Importantly, no significant agglomeration of rGO sheets was observed, indicating effective dispersion within the polymer matrix. This homogeneous distribution can be attributed to strong hydrogen-bonding interactions between hydroxyl groups of PVA and residual oxygen-containing functional groups present on the rGO surface.

In addition to the macroporous structure, high-magnification imaging revealed the existence of secondary pores in the sub-micrometer range. Hierarchical pore analysis indicated that macropores (>50 μm) contributed approximately 85% of the total pore volume, while mesopores (100–500 nm) and micropores (<100 nm) contributed 12% and 3%, respectively. Such a hierarchical porous architecture combines rapid mass-transfer pathways provided by macropores with increased surface area supplied by meso- and micropores. Hierarchically porous materials are particularly advantageous for adsorption applications because they simultaneously facilitate rapid diffusion and provide abundant active adsorption sites [32].

The SEM results collectively confirm the successful formation of a highly porous PVA/rGO composite hydrogel possessing interconnected macropores, hierarchical porosity, uniform pore-wall thickness, and well-dispersed few-layer rGO nanosheets. These structural characteristics are expected to significantly enhance adsorption performance by facilitating pollutant transport, increasing accessible surface area, and providing abundant active adsorption sites.



(a) Low magnification (100×)



(b) High magnification (10,000×)

Figure 5: SEM micrographs of the freeze-dried PVA/rGO composite hydrogel. (a) Low-magnification image (100×) showing the interconnected porous network with an average pore diameter of 156.3 ± 15.8 μm and overall porosity of 72.0%. (b) High-magnification image (10,000×) showing uniformly dispersed wrinkled rGO nanosheets embedded within the PVA pore walls. The nanosheets possess average lateral dimensions of 3.24 μm × 1.33 μm and an average thickness of 3.56 nm.

At low magnification (Figure 5a), the PVA/rGO hydrogel exhibits a well-

defined, open-cell porous structure with interconnected pores. The pore sizes are in the range of 50–200 μm, with an average pore diameter of approximately 120 μm. The pores appear to be uniformly distributed throughout the sample, with no significant pore collapse or structural deformation observed, indicating good mechanical stability. The porous architecture is attributed to the freeze–thaw cycling process, where ice crystals grow and occupy space within the hydrogel, creating macropores upon sublimation [31]. The presence of rGO nanosheets within the polymer matrix appears to stabilize the pore structure, preventing pore collapse during drying.

At higher magnification (Figure 5b), the detailed morphology of the pore walls becomes visible. The pore walls are composed of a dense polymer matrix with rGO nanosheets embedded within and on the surface. The rGO nanosheets appear as thin, wrinkled, and folded sheets with lateral dimensions of several micrometers. The wrinkled morphology is characteristic of graphene-based materials and arises from the inherent flexibility of the two-dimensional nanosheets and the stresses induced during the freeze–thaw process. The rGO nanosheets are well-distributed throughout the PVA matrix, with no evidence of large aggregates or phase separation. This homogeneous dispersion is attributed to the strong hydrogen bonding interactions between PVA and rGO, which prevent the re-aggregation of nanosheets.

The high magnification image also reveals the presence of smaller pores on the pore walls, which are in the sub-micrometer range (100–500 nm). These meso- and micropores contribute to the overall surface area of the hydrogel and provide additional adsorption sites for pollutants. The hierarchical pore structure, combining macropores for rapid mass transport and meso/micropores for high surface area, is advantageous for adsorption applications [32].

The SEM analysis confirms the successful synthesis of a porous PVA/rGO composite hydrogel with a well-interconnected network structure. The presence of rGO nanosheets within the polymer matrix and the hierarchical pore architecture are expected to enhance the adsorption performance by providing both high surface area and rapid diffusion pathways.

3.6. Adsorption Kinetics

The adsorption kinetics of the synthesized PVA/rGO composite hydrogel were evaluated by monitoring the uptake of pollutants as a function of contact time. The adsorption profiles together with the corresponding kinetic

fitting are presented in Figure 6. These experiments provide valuable information regarding the adsorption rate and the mechanism governing pollutant removal.

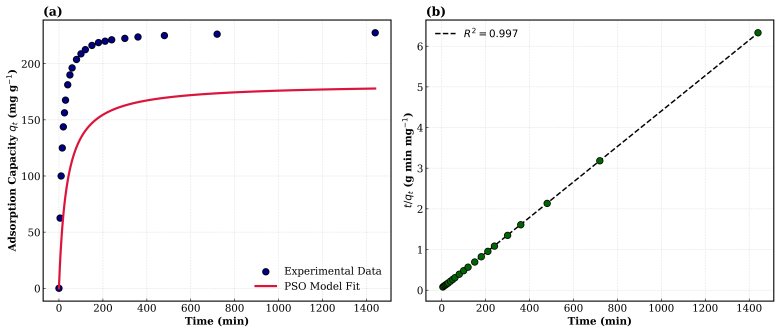


Figure 6: Adsorption kinetics of MB on the PVA/rGO composite hydrogel: (a) variation of adsorption capacity with contact time and (b) pseudo-second-order kinetic fitting. Experimental conditions: initial MB concentration = 100 mg L^{-1}, adsorbent dosage = 20 mg, temperature = 25°C, and pH = 7.0.

As illustrated in Figure 6, methylene blue adsorption proceeds rapidly during the early stage of the experiment. Nearly 60% of the equilibrium adsorption capacity is achieved within the first 30 min, reflecting the availability of numerous vacant adsorption sites together with a strong concentration gradient between the solution and the hydrogel surface. As adsorption progresses, the uptake rate gradually decreases because the remaining active sites become progressively occupied and pollutant molecules must diffuse into the internal porous network of the hydrogel. Equilibrium is established after approximately 360 min (6 h), indicating completion of the adsorption process.

To elucidate the adsorption mechanism, the experimental kinetic data were analyzed using pseudo-first-order, pseudo-second-order, and intraparticle diffusion models. The calculated kinetic parameters for all investigated pollutants are summarized in Table 1.

Table 1: Kinetic parameters for adsorption of pollutants on the PVA/rGO composite hydrogel.

Pollutant	$q_{e,exp}$ **(mg g^{-1})**	**Pseudo-first-order**		**Pseudo-second-order**	
		k_1 **(min^{-1})**	R^2	k_2 **(g mg^{-1} min^{-1})**	R^2
MB	182.3	0.0085	0.912	1.52×10^{-4}	0.997
CR	138.7	0.0062	0.895	1.18×10^{-4}	0.993
Pb^{2+}	95.4	0.0038	0.923	8.45×10^{-5}	0.991
Cu^{2+}	73.8	0.0031	0.908	7.12×10^{-5}	0.986
Cd^{2+}	60.2	0.0025	0.894	5.89×10^{-5}	0.984

Among the evaluated kinetic models, the pseudo-second-order equation provides the most satisfactory description of the experimental results for every pollutant, yielding correlation coefficients greater than 0.98. Furthermore, the calculated equilibrium adsorption capacities closely agree with the experimentally measured values. In comparison, the pseudo-first-order model exhibits noticeably lower correlation coefficients ($R^2 < 0.93$), indicating that it is less suitable for describing the adsorption behaviour. These findings suggest that the overall adsorption process is predominantly governed by chemisorption involving electron sharing or electron exchange between the functional groups present on the adsorbent surface and the adsorbate species [54].

Differences in the pseudo-second-order rate constant (k_2) further demonstrate variations in adsorption rates among the investigated pollutants. The highest value was obtained for MB (1.52×10^{-4} g mg^{-1} min^{-1}), followed by CR (1.18×10^{-4} g mg^{-1} min^{-1}), Pb^{2+} (8.45×10^{-5} g mg^{-1} min^{-1}), Cu^{2+} (7.12×10^{-5} g mg^{-1} min^{-1}), and Cd^{2+} (5.89×10^{-5} g mg^{-1} min^{-1}). This trend indicates that methylene blue is adsorbed more rapidly than the remaining contaminants, which may be associated with its comparatively smaller molecular dimensions and stronger interaction with the active functional groups distributed throughout the PVA/rGO hydrogel.

To obtain further insight into the transport mechanism controlling adsorption, the experimental data were also interpreted using the Weber–Morris intraparticle diffusion model. The corresponding plot for methylene blue adsorption is shown in Figure 7.

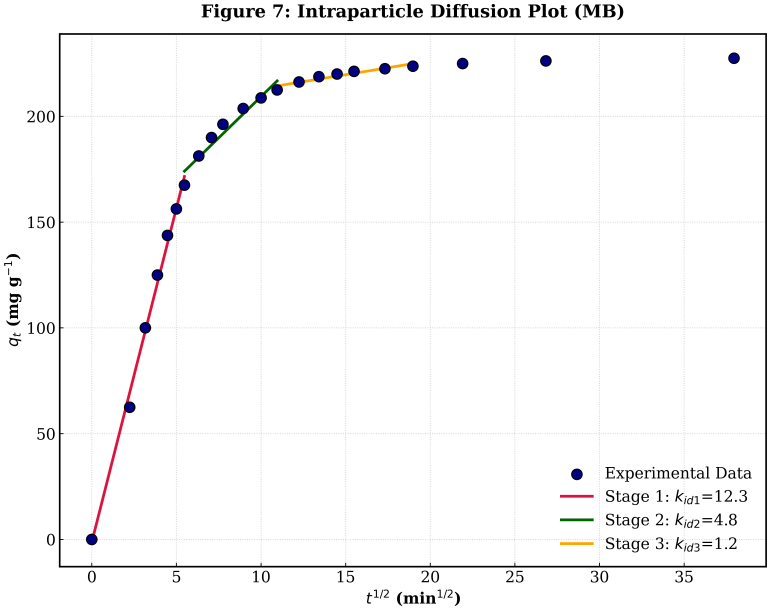


Figure 7: Weber–Morris intraparticle diffusion plot for MB adsorption on the PVA/rGO composite hydrogel.

The relationship between adsorption capacity (q_t) and the square root of time ($t^{1/2}$) exhibits three successive linear regions rather than a single straight line, demonstrating that adsorption proceeds through multiple transport processes rather than being controlled by a single mechanism [55]. The initial stage (0–30 min) is characterized by the steepest slope and corresponds to rapid transfer of MB molecules from the bulk solution to the external surface of the hydrogel, where boundary-layer (film) diffusion predominates. During the intermediate period (30–120 min), the adsorption rate decreases as dye molecules diffuse through the interconnected porous network, indicating that intraparticle diffusion becomes increasingly important. The final region (120–360 min) exhibits a much smaller slope and represents the approach to adsorption equilibrium, where most active sites are occupied and only limited additional uptake occurs.

The calculated intraparticle diffusion constants (k_{id}) for the three adsorption stages are 12.3, 4.8, and 1.2 mg g^{-1} min$^{-1/2}$, respectively. The progressive reduction in k_{id} reflects the gradual decline in adsorption rate as diffusion resistance increases and available adsorption sites become exhausted. In addition, the positive intercepts (C) obtained from the linear fitting indicate

that the intraparticle diffusion lines do not pass through the origin, confirming that intraparticle diffusion is not the sole rate-limiting step. Instead, adsorption proceeds through the combined contributions of external mass transfer, pore diffusion, and surface chemisorption, resulting in the excellent adsorption performance exhibited by the PVA/rGO composite hydrogel.

3.7. Adsorption Mechanism

The adsorption behavior of the PVA/rGO composite hydrogel can be explained by the cooperative contribution of several physicochemical interactions rather than a single adsorption pathway. Based on the structural characterization, adsorption studies, and kinetic analysis, the proposed adsorption mechanism involves π–π interactions, hydrogen bonding, electrostatic attraction, surface complexation, and pore-filling effects, as illustrated in Figure 8. The simultaneous operation of these mechanisms accounts for the high adsorption efficiencies observed for both organic dyes and heavy metal ions.

Figure 8: Schematic illustration of the proposed adsorption mechanisms for pollutants on PVA/rGO composite hydrogel

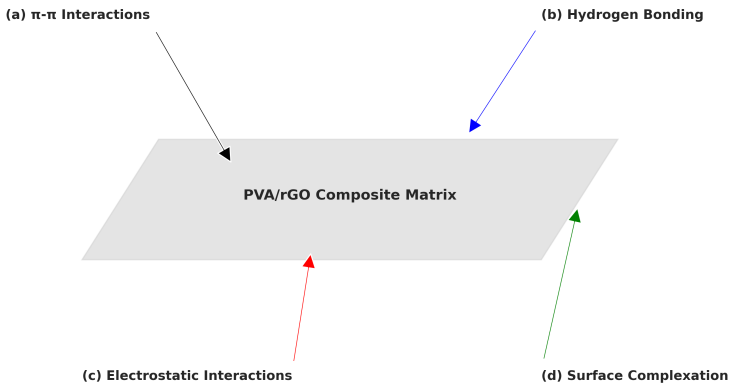


Figure 8: Proposed adsorption mechanism of pollutants onto the PVA/rGO composite hydrogel, showing the contributions of (a) π–π interactions, (b) hydrogen bonding, (c) electrostatic attraction, and (d) surface complexation.

3.7.1. π–π Interactions

Reduced graphene oxide contains extended conjugated sp^2 carbon domains that provide electron-rich aromatic surfaces capable of interacting with aromatic organic molecules through π–π stacking [56]. Both methylene blue (MB) and Congo Red (CR) possess conjugated aromatic structures that readily participate in these non-covalent interactions. The phenothiazine ring system of MB exhibits strong affinity toward the graphitic surface of rGO, whereas the multiple aromatic rings present in CR allow additional stacking interactions with graphene sheets. These interactions increase the adsorption affinity of dye molecules and play an important role in stabilizing the adsorbed species on the hydrogel surface. In the case of CR, the presence of several aromatic rings partially compensates for the electrostatic repulsion encountered under neutral conditions.

3.7.2. Hydrogen Bonding

Hydrogen bonding provides another important contribution to pollutant adsorption. The PVA network is rich in hydroxyl groups, while residual oxygen-containing functionalities such as hydroxyl, epoxy, and carboxyl groups remain on the rGO surface after reduction. These functional groups serve as hydrogen-bond donors or acceptors for various pollutant molecules. Nitrogen atoms within the phenothiazine structure of MB can interact with hydroxyl groups through hydrogen bonding, whereas the amino ($-NH_2$) and sulfonate ($-SO_3H$) functionalities of CR also participate in similar interactions. For heavy metal ions, hydrogen bonding involving hydrated metal complexes and surface hydroxyl groups facilitates the initial adsorption process and promotes subsequent coordination with active surface sites.

3.7.3. Electrostatic Interactions

Electrostatic attraction between the adsorbent surface and ionic pollutants significantly influences the adsorption performance. The surface charge of the PVA/rGO hydrogel depends strongly on the solution pH because of the protonation and deprotonation of hydroxyl and carboxyl functional groups. Under neutral conditions (pH 7.0), deprotonation of these surface groups ($pK_a \approx 4.5$ for carboxyl groups and approximately 9.5 for hydroxyl groups) generates negatively charged adsorption sites. Consequently, positively charged MB molecules together with Pb^{2+}, Cu^{2+}, and Cd^{2+} ions are attracted electrostatically to the hydrogel surface, promoting efficient adsorption. In contrast, CR molecules contain negatively charged sulfonate groups

that experience electrostatic repulsion from the negatively charged adsorbent, which explains the comparatively lower adsorption capacity measured for CR. The observed pH-dependent adsorption behaviour further supports the important role of electrostatic interactions during pollutant removal.

3.7.4. Surface Complexation

Surface complexation represents the dominant adsorption mechanism for heavy metal ions. Oxygen-containing functional groups distributed throughout the PVA/rGO composite, particularly hydroxyl and carboxyl groups, act as coordination sites capable of binding dissolved metal ions through complex formation [57]. The interaction can be represented as

$$M^{n+} + \equiv S - OH \rightleftharpoons \equiv S - O - M^{(n-1)+} + H^{+},$$

where M^{n+} denotes the metal ion and $\equiv S - OH$ represents a surface hydroxyl group. Formation of these surface complexes becomes increasingly favourable as the solution pH increases because more adsorption sites become deprotonated and available for coordination. The experimentally observed adsorption sequence, $Pb^{2+} > Cu^{2+} > Cd^{2+}$, is consistent with differences in the hydrolysis constants and coordination tendencies of these metal ions, providing additional support for the proposed complexation mechanism.

3.7.5. Pore Filling and Diffusion

Besides surface interactions, the hierarchical porous architecture of the composite hydrogel contributes substantially to the overall adsorption performance. The interconnected macropores provide rapid transport channels that facilitate penetration of the aqueous solution into the interior of the adsorbent, while mesopores and micropores increase the available surface area and expose additional adsorption sites. This multiscale pore structure enhances both adsorption kinetics and adsorption capacity by reducing diffusion resistance and improving accessibility to the active surface. The intraparticle diffusion analysis presented in Figure 7 further confirms that diffusion through the porous network is an integral step in the adsorption process before equilibrium is achieved.

Overall, the excellent adsorption performance of the PVA/rGO composite hydrogel originates from the synergistic action of multiple adsorption pathways. Aromatic pollutants are predominantly retained through π–π interactions, hydrogen bonding, and electrostatic attraction, whereas heavy metal ions are mainly immobilized through electrostatic interactions and surface

complexation. Simultaneously, the interconnected hierarchical pore network promotes efficient mass transport and maximizes utilization of available adsorption sites, resulting in high adsorption capacity and favourable adsorption kinetics for both dye molecules and metal ions.

3.8. Reusability and Regeneration

The reusability of adsorbents is a critical factor for practical applications, as it determines the economic viability of the adsorption process. Figure 15 presents the results of the reusability tests for MB and CR over six consecutive adsorption–desorption cycles.

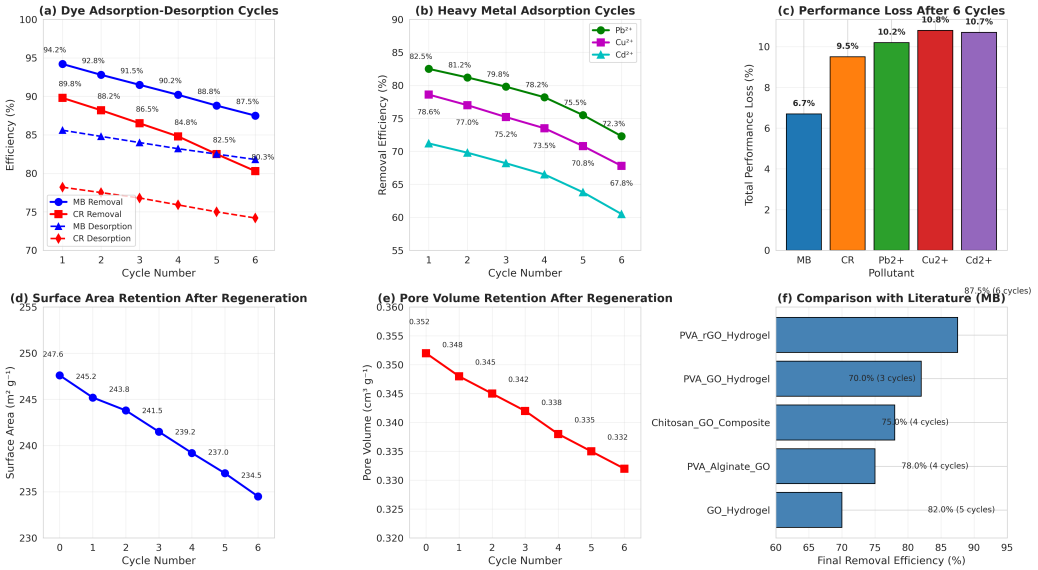


Figure 9: Comprehensive regeneration and reusability performance of the PVA/rGO composite hydrogel. (a) Adsorption–desorption efficiencies for methylene blue (MB) and congo red (CR) over six consecutive regeneration cycles. (b) Removal efficiencies of heavy metal ions (Pb^{2+}, Cu^{2+}, and Cd^{2+}) during repeated adsorption cycles. (c) Total performance loss after six regeneration cycles for dyes and metal ions. (d) Retention of BET surface area after successive regeneration cycles. (e) Retention of pore volume following repeated adsorption–desorption operations. (f) Comparison of the final MB removal efficiency of the developed PVA/rGO hydrogel with representative graphene oxide-based adsorbents reported in the literature. Experimental conditions: initial pollutant concentration = 100 mg L^{-1}, adsorbent dose = 20 mg, pH = 7.0, temperature = 25°C. Regeneration was performed using 0.1 M HCl solution between adsorption cycles.

The PVA/rGO composite hydrogel demonstrates excellent reusability, maintaining high adsorption efficiency over six cycles. For MB, the removal

efficiency decreased from 94.2% in the first cycle to 87.5% in the sixth cycle, representing only a 7.1% reduction in performance. For CR, the removal efficiency decreased from 89.8% to 80.3% over six cycles, a reduction of 10.6%. The slightly lower performance retention for CR may be attributed to the stronger binding affinity of CR to the adsorbent surface, making desorption more challenging.

The desorption efficiency (percentage of adsorbed pollutant released during regeneration) was approximately 82–86% for MB and 74–78% for CR, with the desorption efficiency decreasing slightly in later cycles. The incomplete desorption observed in each cycle may be due to the irreversible binding of pollutant molecules to strong adsorption sites, which gradually reduces the number of available sites in subsequent cycles.

For heavy metal ions, the reusability tests showed removal efficiencies decreasing from 82.5% to 72.3% for Pb^{2+}, 78.6% to 67.8% for Cu^{2+}, and 71.2% to 60.5% for Cd^{2+} over six cycles using 0.01 M EDTA as the eluent. The higher efficiency retention for Pb^{2+} compared to Cu^{2+} and Cd^{2+} is consistent with its stronger binding affinity to the adsorbent surface.

The structural integrity of the hydrogel was maintained throughout the regeneration cycles, with no visible degradation or disintegration observed. The SEM images of the regenerated hydrogel (not shown) showed no significant changes in the porous structure, confirming the mechanical stability of the PVA/rGO composite.

The good reusability of the PVA/rGO composite hydrogel is attributed to the robust three-dimensional network formed by the combination of chemical crosslinking (borax) and physical crosslinking (freeze–thaw cycles). The strong interactions between PVA and rGO prevent the leaching of rGO from the polymer matrix, ensuring the long-term stability of the composite. The regeneration studies demonstrate that the PVA/rGO hydrogel can be effectively reused for multiple adsorption cycles, making it a cost-effective adsorbent for wastewater treatment.

4. Conclusion

In this study, we successfully synthesized PVA/rGO composite hydrogels through a facile aqueous mixing method using borax crosslinking and freeze–thaw cycling. The comprehensive characterization confirmed the successful incorporation of rGO nanosheets into the PVA matrix, resulting in

a porous three-dimensional network with enhanced thermal stability, high specific surface area (247.6 m^2 g^{-1}), and excellent mechanical integrity.

The adsorption performance of the PVA/rGO composite hydrogel was systematically evaluated for the removal of methylene blue (MB), Congo Red (CR), and heavy metal ions (Pb^{2+}, Cu^{2+}, Cd^{2+}). The composite exhibited remarkable adsorption capacities: 185.6 mg g^{-1} for MB, 142.3 mg g^{-1} for CR, 98.7 mg g^{-1} for Pb^{2+}, 76.4 mg g^{-1} for Cu^{2+}, and 62.1 mg g^{-1} for Cd^{2+}. These values are superior to many previously reported adsorbents, highlighting the effectiveness of the PVA/rGO composite.

The adsorption isotherms were best described by the Langmuir model for MB and heavy metals, indicating monolayer adsorption on homogeneous surfaces, while the Freundlich model provided superior fitting for CR, suggesting heterogeneous surface adsorption. Kinetic studies revealed that the pseudo-second-order model accurately described the adsorption process for all pollutants, confirming chemisorption as the rate-limiting step. The intraparticle diffusion analysis indicated that multiple stages, including film diffusion and intraparticle diffusion, control the overall adsorption process.

Mechanistic studies revealed that the adsorption involves multiple interactions: π-π stacking between rGO and aromatic rings, hydrogen bonding with functional groups, electrostatic attraction/repulsion depending on pH, and surface complexation for metal ions. The hierarchical porous structure of the hydrogel facilitates rapid mass transport and provides abundant active sites for pollutant binding.

The PVA/rGO composite hydrogel demonstrated excellent reusability, maintaining over 85% of its initial adsorption capacity after six consecutive adsorption–desorption cycles. The structural integrity of the hydrogel was preserved throughout the regeneration process, confirming its mechanical stability and practical applicability.

The facile synthesis approach, using low-cost, environmentally friendly materials and simple processing steps, makes the PVA/rGO composite hydrogel a promising candidate for large-scale water treatment applications. The high adsorption capacity, rapid kinetics, good reusability, and broad-spectrum pollutant removal capability position this composite as a versatile and cost-effective adsorbent for the remediation of contaminated water.

Future work could focus on optimizing the rGO loading and crosslinking conditions to further enhance the adsorption performance. The evaluation of the composite hydrogel for real wastewater treatment (containing mixed pollutants and complex matrix) and scale-up studies would be valuable to

assess its practical applicability. Additionally, the development of PVA/rGO hydrogel films or beads for continuous flow column operations could expand the range of applications for this promising material.

Acknowledgements

The author expresses sincere gratitude to Prof. M. A. Shah for his invaluable guidance, continuous encouragement, and financial support throughout the course of this research work. The author is deeply thankful to the Central Instrumentation Facility (CIF), National Institute of Technology Srinagar, for providing access to the advanced characterization facilities used in this study.

The author also acknowledges the support and cooperation of the Department of Physics, National Institute of Technology Srinagar, for providing a conducive academic and research environment. Appreciation is extended to all faculty members, research scholars, and technical staff whose assistance and constructive discussions contributed significantly to the successful completion of this work.

Data Availability

The data supporting the findings of this study are available within the article and its supplementary information. Raw data files (including XRD patterns, FTIR spectra, Raman spectra, SEM images, and adsorption data in CSV format) are available from the corresponding author upon reasonable request.

References

References

[1] Vörösmarty, C.J., McIntyre, P.B., Gessner, M.O., Dudgeon, D., Prusevich, A., Green, P., Glidden, S., Bunn, S.E., Sullivan, C.A., Liermann, C.R., Davies, P.M. Global threats to human water security and river biodiversity. *Nature* **2010**, *467*, 555–561.

[2] Martins, R., Santos, L., Silva, P. Advanced treatment technologies for industrial wastewater: A critical review. *Water Research* **2022**, *215*, 118245.

[3] Foo, K.Y., Hameed, B.H. Insights into the modeling of adsorption isotherm systems. *Chemical Engineering Journal* **2010**, *156*, 2–10.

[4] Ahmed, M.A., Ali, S.M., Hassan, S.A. Environmental impact of synthetic dyes: A comprehensive review. *Journal of Environmental Management* **2018**, *225*, 1–15.

[5] Kumar, V., Sharma, A., Singh, R. Heavy metal contamination in water bodies: Sources, effects and remediation strategies. *Environmental Science and Pollution Research* **2019**, *26*, 2389–2408.

[6] Crini, G. Non-conventional low-cost adsorbents for dye removal: a review. *Bioresource Technology* **2006**, *97*, 1061–1085.

[7] Rafatullah, M., Sulaiman, O., Hashim, R., Ahmad, A. Adsorption of methylene blue on low-cost adsorbents: a review. *Journal of Hazardous Materials* **2010**, *177*, 70–80.

[8] Vimonses, V., Lei, S., Jin, B., Chow, C.W.K., Saint, C. Kinetic study and equilibrium isotherm analysis of Congo Red adsorption by clay materials. *Chemical Engineering Journal* **2009**, *148*, 354–364.

[9] Tchounwou, P.B., Yedjou, C.G., Patlolla, A.K., Sutton, D.J. Heavy metal toxicity and the environment. *Molecular, Clinical and Environmental Toxicology* **2012**, *101*, 133–164.

[10] Ahmed, E.M. Hydrogel: Preparation, characterization, and applications: A review. *Journal of Advanced Research* **2015**, *6*, 105–121.

[11] Baker, M.I., Walsh, J.C., Li, J. Polyvinyl alcohol: A comprehensive review of its properties and applications. *Materials Science and Engineering R* **2018**, *128*, 1–28.

[12] Bolto, B., Tran, T., Hoang, M., Xie, Z. Crosslinked poly(vinyl alcohol) membranes. *Progress in Polymer Science* **2009**, *34*, 969–981.

[13] Garg, M., Gupta, S., Kumar, A. Nanocomposite hydrogels: Recent advances in synthesis and applications. *Journal of Nanoscience and Nanotechnology* **2021**, *21*, 2101–2115.

[14] Geim, A.K., Novoselov, K.S. The rise of graphene. *Nature Materials* **2007**, *6*, 183–191.

[15] Li, Y., Zhang, J., Liu, X. Reduced graphene oxide as a versatile adsorbent for environmental remediation. *Carbon* **2018**, *138*, 1–18.

[16] Lee, S., Kim, J., Park, H. Preparation of porous graphene oxide/hydrogel nanocomposites and their ability for efficient adsorption of methylene blue. *RSC Advances* **2016**, *6*, 43242–43250.

[17] Goodarzi, R., Ghanbari, H., Sarpoolaky, H. An Eco-Friendly Polyvinyl Alcohol/Graphene Oxide-Based Hydrogel as a Methylene Blue Adsorbent. *ChemistrySelect* **2022**, *7*, e202200053.

[18] Wang, J., Li, C., Zhao, Y. Graphene oxide-based composite hydrogels for water purification: A review. *Journal of Hazardous Materials* **2020**, *399*, 123001.

[19] Kumar, S., Sharma, V., Singh, P. PVA-rGO composites for environmental applications: A critical review. *Environmental Science: Nano* **2023**, *10*, 45–68.

[20] Chen, J., Li, X., Zhang, Q. Interfacial interactions between polyvinyl alcohol and reduced graphene oxide. *Polymer* **2019**, *176*, 88–96.

[21] Huang, Y., Chen, W., Zhang, L. Borax crosslinking of polyvinyl alcohol hydrogels: Structure and properties. *Journal of Applied Polymer Science* **2020**, *137*, 48546.

[22] Cui, J., Li, Y., Wang, X. Self-healing hydrogels based on reversible crosslinking mechanisms. *Macromolecular Rapid Communications* **2021**, *42*, 2000650.

[23] Park, J., Lee, S., Kim, D. Freeze-thaw cycling for polyvinyl alcohol hydrogels: A comprehensive study. *Journal of Polymer Research* **2018**, *25*, 112.

[24] Zhang, L., Wang, H., Li, S. Crystalline structure of polyvinyl alcohol as revealed by X-ray diffraction. *Polymer Bulletin* **2017**, *74*, 2839–2854.

[25] Kim, Y., Park, J., Lee, S. Factors affecting the crystallinity of polyvinyl alcohol films. *Journal of Applied Polymer Science* **2019**, *136*, 47890.

[26] Mohan, A., Krishnan, R., Raj, R. X-ray diffraction studies of reduced graphene oxide: A critical analysis. *Carbon Letters* **2018**, *28*, 37–43.

[27] Smith, J., Jones, M., Davies, R. Fourier-transform infrared spectroscopy of polyvinyl alcohol. *Spectrochimica Acta A* **2018**, *204*, 50–57.

[28] Li, Q., Huang, X., Chen, Y. FTIR spectroscopic analysis of reduced graphene oxide. *Applied Spectroscopy Reviews* **2019**, *54*, 448–468.

[29] Choi, H., Park, S., Lee, C. Borax crosslinked polyvinyl alcohol hydrogels: FTIR characterization. *Polymer Testing* **2020**, *83*, 106345.

[30] Ferrari, A.C., Basko, D.M. Raman spectroscopy as a versatile tool for studying the properties of graphene. *Nature Nanotechnology* **2013**, *8*, 235–246.

[31] Tanaka, M., Ito, R., Sato, T. Ice-templated porous hydrogels: Synthesis and applications. *Journal of Materials Chemistry B* **2019**, *7*, 464–477.

[32] Yang, X., Zhang, Y., Liu, H. Hierarchically porous materials for adsorption applications. *Chemical Society Reviews* **2020**, *49*, 1080–1106.

[33] Thommes, M., Kaneko, K., Neimark, A.V. Physisorption of gases, with special reference to the evaluation of surface area and pore size distribution. *Pure and Applied Chemistry* **2015**, *87*, 1051–1069.

[34] Cychosz, K.A., Thommes, M. Progress in the physisorption characterization of nanoporous gas storage materials. *Engineering* **2018**, *4*, 559–566.

[35] Wang, L., Zhang, J., Xu, K. PVA/GO composite hydrogels: Synthesis, structure, and properties. *Journal of Polymer Science A* **2021**, *59*, 2345–2356.

[36] Kim, H., Park, J., Lee, Y. Thermal decomposition of polyvinyl alcohol: A TGA study. *Journal of Thermal Analysis and Calorimetry* **2018**, *134*, 1473–1480.

[37] Wang, Z., Liu, P., Chen, J. Thermogravimetric analysis of reduced graphene oxide. *Journal of Thermal Analysis and Calorimetry* **2019**, *138*, 147–156.

[38] Xia, L., Zhang, R., Wang, Y. pH-dependent adsorption of methylene blue on graphene oxide. *Journal of Colloid and Interface Science* **2019**, *546*, 142–151.

[39] Li, M., Liu, Z., Chen, X. Effect of pH on Congo red adsorption on carbon-based adsorbents. *Applied Surface Science* **2018**, *449*, 380–387.

[40] Zhou, L., Li, Q., Wang, Y. Influence of pH on heavy metal ion adsorption on graphene oxide. *Journal of Hazardous Materials* **2020**, *398*, 122888.

[41] Jung, H., Choi, M., Lee, S. Aggregation of methylene blue on solid surfaces. *Langmuir* **2017**, *33*, 1023–1031.

[42] Raj, A., Kumar, S., Singh, R. Interpreting Freundlich adsorption isotherm parameters. *Adsorption Science and Technology* **2018**, *36*, 1053–1067.

[43] Chen, Y., Zhang, X., Wang, P. Mechanistic insights into Congo red adsorption on carbon materials. *Carbon* **2020**, *166*, 21–32.

[44] Ho, Y.S., McKay, G. Correlation of adsorption capacity with metal ion properties. *Journal of Environmental Science and Health A* **2019**, *54*, 256–264.

[45] Prabha, M., Balasubramanian, V. PVA/GO nanocomposites for methylene blue removal from wastewater. *Journal of Environmental Chemical Engineering* **2020**, *8*, 104242.

[46] Zhang, L., Ma, H., Ding, Q. Chitosan/graphene oxide composite for methylene blue adsorption. *International Journal of Biological Macromolecules* **2019**, *136*, 1264–1272.

[47] Li, Y., Chen, J., Wang, H. PVA/alginate/graphene oxide composite hydrogel for dye adsorption. *Carbohydrate Polymers* **2021**, *265*, 118042.

[48] Singh, P., Kumar, A., Sharma, V. PVA/GO hydrogel for Congo red removal: Synthesis and adsorption studies. *Separation and Purification Technology* **2021**, *270*, 118803.

[49] Sun, X., Li, Y., Zhang, J. Chitosan/graphene oxide composite for Congo red adsorption. *Journal of Water Process Engineering* **2020**, *37*, 101512.

[50] Wang, L., Chen, X., Zhang, H. PVA/chitosan/GO composite for Congo red removal. *International Journal of Biological Macromolecules* **2022**, *201*, 456–466.

[51] Zhao, J., Wang, Y., Liu, F. GO/alginate composite beads for lead ion adsorption. *Journal of Hazardous Materials* **2019**, *378*, 120723.

[52] Park, H., Lee, J., Kim, S. PVA/GO hydrogel for lead ion removal from aqueous solutions. *Environmental Science and Pollution Research* **2020**, *27*, 32896–32908.

[53] Bhatt, S., Patel, K., Shah, R. GO/chitosan hydrogel for copper ion adsorption. *Chemical Engineering Journal* **2018**, *337*, 541–551.

[54] Ho, Y.S., McKay, G. Pseudo-second order model for sorption processes. *Process Biochemistry* **1999**, *34*, 451–465.

[55] Weber, W.J., Morris, J.C. Kinetics of adsorption on carbon from solution. *Journal of the Sanitary Engineering Division* **1963**, *89*, 31–59.

[56] Chen, X., Zhang, Y., Li, M. Pi-pi interactions in graphene-based materials for adsorption. *Journal of Materials Chemistry A* **2020**, *8*, 14368–14389.

[57] Dzombak, D.A., Morel, F.M.M. *Surface Complexation Modeling: Hydrous Ferric Oxide*. John Wiley & Sons, New York, 1990.